

A new method for ISOCAM data reduction – II. Mid-infrared extragalactic source counts in the ELAIS Southern field

C. Gruppioni,^{1,2★} C. Lari,³ F. Pozzi,^{2,4} G. Zamorani,² A. Franceschini,⁵
S. Oliver,⁶ M. Rowan-Robinson⁷ and S. Serjeant⁸

¹*Istituto Nazionale di Astrofisica, Osservatorio Astronomico di Padova, vicolo dell'Osservatorio 5, I-35122 Padova, Italy*

²*Istituto Nazionale di Astrofisica, Osservatorio Astronomico di Bologna, via Ranzani 1, I-40127 Bologna, Italy*

³*Istituto di Radioastronomia del CNR, via Gobetti 101, I-40129 Bologna, Italy*

⁴*Dipartimento di Astronomia, Università di Bologna, via Ranzani 1, I-40127 Bologna, Italy*

⁵*Dipartimento di Astronomia, Università di Padova, vicolo dell'Osservatorio 2, I-35122 Padova, Italy*

⁶*Astronomy Centre, CPES, University of Sussex, Falmer, Brighton BN1 9QJ*

⁷*Imperial College of Science, Technology and Medicine, Prince Consort Road, London SW7 2BZ*

⁸*Unit for Space Sciences and Astrophysics, School of Physical Sciences, University of Kent, Canterbury CT2 7NR*

Accepted 2002 May 9. Received 2002 May 7; in original form 2002 February 19

ABSTRACT

We present the 15- μm extragalactic source counts from the Final Analysis Catalogue of the European Large Area *ISO* Survey (ELAIS) Southern hemisphere field S1, extracted using the Lari method. The large number of extragalactic sources (~ 350) detected over this area between about 0.5 and 100 mJy guarantee a high statistical significance of the source counts in the previously poorly covered flux density range between *IRAS* and the Deep ISOCAM Surveys. The bright counts in S1 ($S_{15\mu\text{m}} \gtrsim 2$ mJy) are significantly lower than other published ISOCAM counts in the same flux range and are consistent with a flat, Euclidean slope, suggesting the dominance of a non-evolving population. In contrast, at fainter fluxes ($S_{15\mu\text{m}} \lesssim 2$ mJy) our counts show a strong departure from no-evolution models, with a very steep super-Euclidean slope down to our flux limit (~ 0.5 mJy). Strong luminosity and density evolutions of the order of, respectively, $L \propto (1+z)^{3.0}$ and $\rho \propto (1+z)^{3.5}$ are needed at least for the population of star-forming galaxies in order to fit the counts and the redshift distributions observed at different fluxes. A luminosity break around $10^{10.8} L_{\odot}$ must be introduced in the local luminosity function of starburst galaxies in order to reproduce our sharp increase of the counts below 2 mJy and the redshift distributions observed for 15- μm sources at different flux levels. The contribution of the strongly evolving starburst population (down to 50 μJy) to the 15- μm cosmic background is estimated to be $\sim 2.2 \text{ nW m}^{-2} \text{ sr}^{-1}$, which corresponds to ~ 67 per cent of the total mid-infrared background estimate.

Key words: methods: data analysis – galaxies: evolution – galaxies: starburst – cosmology: observations – infrared: galaxies.

1 INTRODUCTION

Deep galaxy counts are a key instrument for the study of galaxy evolution, and can provide strong constraints to theoretical models. In fact, the departure of source counts from Euclidean predictions depends on the intrinsic evolution of galaxies and their redshift distribution. In the past few years several deep observations in different wavebands have provided a significant advance in our knowledge of galaxy formation and evolution. Optical surveys found a strong evolution of the population of blue galaxies as a function of red-

shift to $z \sim 1$ (Metcalf et al. 1995; Lilly et al. 1996), while mid- and far-infrared (far-IR) deep surveys (Dole et al. 1999; Elbaz et al. 1999a,b; Elbaz 2000), together with the detection of a substantial diffuse cosmic infrared background (CIRB) in the 300 μm to 1 mm range (Puget et al. 1996; Hauser, Arendt & Kelsall 1998; Fixsen et al. 1998; Lagache et al. 1999), implied a strong evolution also for galaxies emitting in the infrared. In fact, the mid/far-IR extragalactic background is at least as large as the ultraviolet/optical/near-IR background, thus implying a stronger contribution of obscured star formation at redshifts larger than those observed by *IRAS*.

IRAS has sampled the local Universe ($z < 0.2$) in the mid/far-IR band, discovering luminous infrared galaxies (LIGs; $L > 10^{11} L_{\odot}$)

★E-mail: carlotta@avalon.bo.astro.it

that radiate most of their light in the infrared band. Although LIGs are the most luminous starburst galaxies ever detected, they are relatively rare in the local Universe, thus making up only a small fraction of the total energy output from galaxies (Soifer & Neugebauer 1991). However, different analyses of the *IRAS* extragalactic source counts by Hacking, Houck & Condon (1987), Lonsdale & Hacking (1989), Saunders et al. (1990) and Kim & Sanders (1998) have shown some evidence for strong evolution at low flux density levels for ultraluminous infrared galaxies (ULIGs; $L_{\text{bol}} \simeq L_{\text{IR}} > 10^{12} L_{\odot}$). Owing to the small redshift range sampled by *IRAS*, these results can only be indicative, though the suggestion that ULIGs might have played a stronger role in the past is supported by the detection of the strong infrared background.

With 1000 times better sensitivity and 60 times better resolution than *IRAS*, the ISOCAM instrument (Cesarsky et al. 1996) on board the *Infrared Space Observatory* (*ISO*; Kessler et al. 1996) has provided deep and ultra-deep mid-infrared extragalactic surveys (mainly with the LW3 filter: 12–18 μm), unveiling most of the star formation in the Universe to $z = 1$. The source counts derived from these deep/ultra-deep surveys (covering the flux density range 0.05–4 mJy) strongly diverge from no-evolution models at fluxes fainter than about 1 mJy, with an increasing difference that reaches a factor of 10 around the faintest limits (0.05–0.1 mJy; Elbaz et al. 1999a,b). The faint mid-infrared sources detected in the deep/ultra-deep ISOCAM surveys have been identified mainly with galaxies at $z \simeq 0.7$ and show LIG-like luminosities (Aussel et al. 1999b; Elbaz et al. 1999a,b; Flores et al. 1999).

Although the deep/ultra-deep ISOCAM surveys have produced crucial results on galaxy evolution in the infrared, having identified most of the galaxies producing the mid-infrared background, there is a large gap in the flux density sampled by these surveys and by the *IRAS* surveys. In particular, the flux density range 4–200 mJy is essentially uncovered in the mid/far-infrared and only a few sources have been detected by the deep ISOCAM surveys in the important flux range 1–4 mJy, where most of the existing evolutionary models (i.e. Xu 2000; Franceschini et al. 2001; Chary & Elbaz 2001; Rowan-Robinson 2001) predict a substantial change in the relative contribution of a local non-evolving and a more distant evolving population. This scarcity of data in this flux interval reflects also in a poor knowledge of the local luminosity function for starburst galaxies and a corresponding uncertainty in the evolutionary properties of the different classes of infrared extragalactic objects.

The European Large Area *ISO* Survey (ELAIS; Oliver et al. 2000) is the largest survey conducted with *ISO* and provides a link between the *IRAS* survey and the deep/ultra-deep ISOCAM surveys. ELAIS is a collaboration between 20 European institutes, and involves a deep, wide-angle survey at high galactic latitudes, at wavelengths of 6.7 μm (LW2), 15 μm (LW3), 90 μm (C100) and 175 μm (C200) with *ISO*. In particular, the 15- μm survey covers a total area of $\sim 12 \text{ deg}^2$, divided into four main fields and several smaller areas. One of the main fields, S1, is located in the Southern hemisphere. The whole S1 area has been surveyed in the radio (at 1.4 GHz, Gruppioni et al. 1999), in several optical bands (La Franca et al., in preparation) and in the hard X-ray with *BeppoSAX* (Alexander et al. 2001). Moreover, spectroscopic information and redshifts are available for a large number of sources (Gruppioni et al. (2001); La Franca et al., in preparation).

We have reduced the 15- μm data in S1 using a new ISOCAM data reduction technique (Lari technique) especially developed for the detection of faint sources, obtaining a catalogue (complete at the 5σ level) of 462 sources in the flux density range 0.45–150 mJy.

Details about the data reduction technique and the source catalogue have been presented in Lari et al. (2001, hereafter Paper I). Here we present the source counts at 15 μm derived from that catalogue.

The paper is structured as follows. In Section 2 we give a brief description of the 15- μm ELAIS survey in S1. In Section 3 we present the completeness and reliability of our sample at different flux levels. In Section 4 we present the sample used to derive the source counts, which are shown in Section 5. Finally, in Sections 6 and 7 we discuss our results and their implications, and present our conclusions.

Throughout this paper we will assume that $H_0 = 50 \text{ km s}^{-1} \text{ Mpc}^{-1}$, $\Omega_m = 0.3$ and $\Omega_\Lambda = 0.7$.

2 DESCRIPTION OF THE ELAIS S1 SURVEY

The ELAIS survey at 15 μm , performed in raster mode with the ISOCAM instrument on board *ISO*, covers a total area of $\sim 12 \text{ deg}^2$ divided into four main fields and several smaller areas. The main field located in the Southern hemisphere (S1) is centred at $\alpha(2000) = 00^{\text{h}}34^{\text{m}}44^{\text{s}}.4$, $\delta(2000) = -43^{\circ}28'12''$ and covers an area of $2 \times 2 \text{ deg}^2$. The 15- μm survey performed in S1 with the ISOCAM instrument consists of nine different rasters. Each raster covers an area of $\sim 43.5 \times 42 \text{ arcmin}^2$; eight of them have been observed once, while one, S1_5, was observed three times.

The 15- μm data have been reduced and analysed using the Lari technique, described in detail in Paper I. With this data reduction method, we have obtained a sample of 462 sources with signal-to-noise ratio ≥ 5 in the flux range 0.45–150 mJy. The fainter sources have been detected in the central raster of S1 (S1_5), whose image has been obtained by combining three single observations centred on the same position. The source catalogue in S1 and the relative parameter errors were presented and discussed in Paper I, together with the detection rates at different flux densities derived with simulations.

The detection rates given in Paper I cannot be directly translated to completeness of the real catalogue, because our simulations were performed at discrete flux values rather than following a continuous flux distribution. However, the results presented in Paper I can be used to obtain the completeness of the catalogue and the source count corrections, as discussed in the next section.

3 COMPLETENESS AND RELIABILITY

3.1 Brief summary of the results and definitions from Paper I

Before describing in detail the method used to derive the completeness of our source counts, it is useful to summarize the more relevant results and definitions of Paper I. The simulations performed in the S1 field provided not only the completeness of our detections at different flux levels, but also the internal calibration of the source photometry and the distribution of the ratio between the measured and the theoretical peak fluxes (crucial for the computations described in the next section).

Here we give some relevant definitions and relations:

- (i) f_s is the peak flux measured on maps for both real and simulated sources. Its value depends both on the data reduction method and on the ELAIS observing strategy plus ISOCAM instrumental effects.
- (ii) f_0 is the ‘theoretical’ peak flux measured on simulated maps containing neither glitches nor noise. Its value depends

only on the ELAIS observing strategy plus ISOCAM instrumental effects.

(iii) $q \equiv f_s/f_0$.

(iv) q_{med} is the peak of the f_s/f_0 distribution (also called systematic flux bias) and is 0.78 ± 0.03 in S1 and 0.82 ± 0.03 in S1.5. These values are used to correct the measured flux densities.

(v) Flux density determination:

$$s = (f_s/f_0)s_0/q_{\text{med}}. \quad (1)$$

For simulations s_0 is the injected total flux, while for real data s_0 is derived through successive iterations starting from a rough estimated value:

$$s_0 = f_s / \langle f_s/s_0 \rangle_{\text{sim}} \quad (2)$$

where $\langle f_s/s_0 \rangle_{\text{sim}} = 0.132$ is the average value resulting from simulations. We can consider s as the measured flux density and s_0 as the ‘true’ flux density of a source.

(vi) The photometric accuracy of our data reduction of the S1 area has been tested using the stars of the field and following the relation calibrated on *IRAS* data by Aussel & Alexander (2001) to predict the fluxes of stars. By a comparison between the predicted fluxes and the ones derived from our analysis, we have obtained a very good agreement and a relative flux scale of 1.096 ± 0.044 (i.e. our fluxes have to be multiplied by 1.096 to be put on the same scale as *IRAS* fluxes).

3.2 The g function

As described in Paper I and mentioned in the previous section, with simulations in S1 we have derived the distribution of measured (f_s) to theoretical (f_0) peak flux ratio. This distribution is crucial in deriving the completeness of the catalogue and the internal flux calibration. To this purpose, we have considered the f_s/f_0 distribution as a model function, hereafter called g function. The g distribution function, obtained for simulated sources, is a combination of an intrinsic g function (referred to as g_0) plus a term due to noise. As a rough estimate of g_0 in Paper I we considered the measured g distribution obtained for 3-mJy simulated sources ($g_{0.3}$). Because 3 mJy is a relatively high flux density (it is the highest flux injected in our simulations), the $g_{0.3}$ distribution is almost unbiased by detection incompleteness, and we can consider it to be a good approximation of the intrinsic one. However, using the same simulation, we have obtained a more refined estimate of the intrinsic g_0 function correcting the observed f_s/f_0 distribution for the low level of detection incompleteness still present at this flux. Our procedure was as follows.

Each detected source i has a $q_i = f_s(i)/f_0(i)$ value. On a different position j , assuming that the $f_s(i)/f_0(i)$ value is not dependent on position, the peak flux would be measured with a value $f_{s,i}(j) = q_i f_0(j)$ and would be detected only if $f_{s,i}(j)$ were greater than five times the local noise, $\sigma(j)$. If N_i is the number of possible detections in all the different j positions of the simulations, the weight to be assigned to the i th source is $1/N_i$. Finally, the estimate of the intrinsic g_0 function in a given interval of q is obtained by summing the weights of all the detected sources with a q value in the same interval. By construction, the integral of g_0 over the entire range of q is unity.

Once the g_0 distribution is obtained, the general g distribution can be derived by convolving g_0 with the distribution of noise, here assumed to be Gaussian. This is possible in the approximation that the measured peak flux f_s is the sum of a ‘true’ value, f_s^t , and a

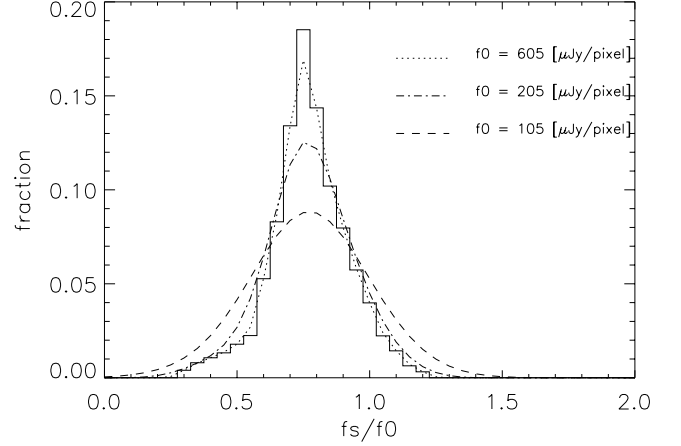


Figure 1. Predicted distributions of the ratio between the measured and the theoretical peak flux, f_s/f_0 (also g function), in the presence of rms noise of $26 \mu\text{Jy pixel}^{-1}$. These distributions, obtained from simulations, are shown for three different average values of f_0 corresponding to different input fluxes. The solid histogram shows the intrinsic g_0 distribution (see text).

stochastic term, χ , due to noise, so that the $q (\equiv f_s/f_0)$ measured value is

$$q = \frac{f_s}{f_0} = \frac{f_s^t}{f_0} + \frac{\chi}{f_0} \quad (3)$$

with the χ term following a Gaussian distribution with average equal to zero and dispersion equal to the rms noise value, σ . Following this formalism, then the g distribution, expressed as a function of f_s/f_0 and f_0/σ , is obtained by just convolving g_0 with the noise distribution, integrating over the possible values of the variable χ :

$$g\left(\frac{f_s}{f_0}, \frac{f_0}{\sigma}\right) = \sqrt{\frac{1}{2\pi}} \frac{1}{\sigma} \int g_0\left(\frac{f_s}{f_0} - \frac{\chi}{f_0}\right) e^{-\chi^2/2\sigma^2} d\chi. \quad (4)$$

In Fig. 1 we show the intrinsic g_0 distribution computed as above (solid histogram) and the predicted distributions of the ratio f_s/f_0 in the presence of a σ of $26 \mu\text{Jy pixel}^{-1}$ (typical of our data) for three different values of f_0 , corresponding to different mean values of f_0 for different total input fluxes. As can be seen, the presence of noise broadens the flux distributions, and this effect becomes stronger towards fainter fluxes (as shown also in fig. 7 of Paper I).

If we assume that the g function reflects all the multiplicative and additive error components due to the data reduction, we can use this function to predict the distribution of the detection rate for both simulated and real sources, as described in the next subsection.

3.3 Completeness

First we have computed the incompleteness introduced by our data reduction method, represented by the loss of sources not accounted for by our model. In fact, sources can be missed by our method if interpreted as background transients. The incompleteness of our method is obtained from simulations by computing the ratio between the number of detections and the number of expected sources in different peak flux intervals, $[f_0 - df_0, f_0 + df_0]$. The number of expected sources is derived by summing together the predicted detection contributions

$$I_i(f_0) = \int_{5\sigma/f_0}^{\infty} g(q, f_0) dq$$

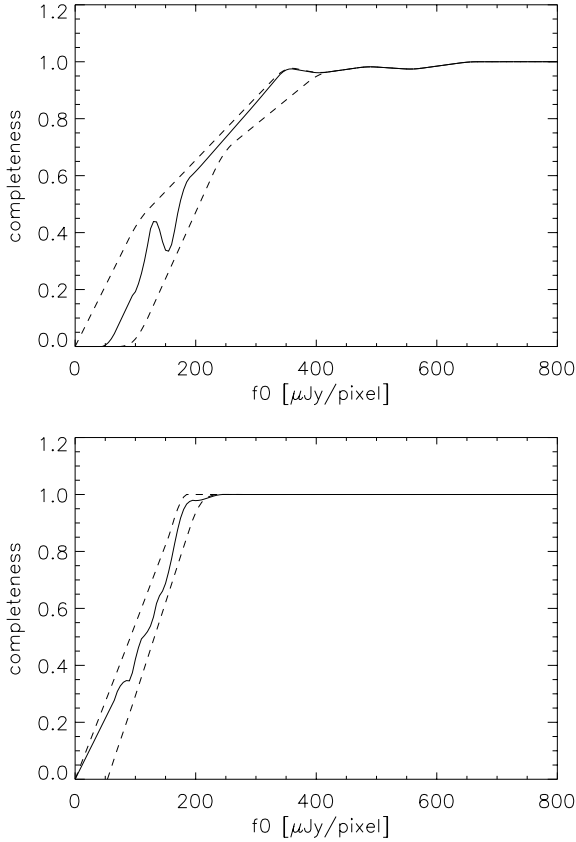


Figure 2. Completeness function of Lari method as function of the theoretical peak flux for S1 (top) and S1.5 (bottom). The dashed lines give an estimate of the lower and upper envelopes of the completeness function.

of all the sources i with peak flux f_{0i} belonging to the same interval:

$$N_{\text{exp}}(f_0) = \sum_{f_{0i} \in [f_0 \pm \Delta f_0]} I_i(f_0). \quad (5)$$

In Fig. 2 the resulting function describing the incompleteness of our method is plotted as a function of f_0 , together with its lower and upper envelopes, for S1 (top panel) and S1.5 (bottom panel).

To obtain the global correction to be applied to our source counts, we need to consider also the areal coverage of our survey (i.e. the fraction of the survey area where a source of peak flux f_s can be detected: $f_s \geq 5\sigma$) and the fact that real sources do not follow a discrete flux distribution as our simulated sources. To account for the latter effect, we have assumed a certain shape to describe the real source counts observed in the sky. According to the published counts at 15 μm (e.g. Elbaz et al. 1999a), we have assumed two power laws between 0.4 and 150 mJy:

$$\frac{dN(s)}{ds} \propto \begin{cases} S^{-\alpha_1} & \text{if } S > 2 \text{ mJy,} \\ S^{-\alpha_2} & \text{if } S < 2 \text{ mJy,} \end{cases} \quad (6)$$

with $\alpha_1 = 2.3$ and $\alpha_2 = 3.0$ as first estimate values.

By weighting the above ‘theoretical’ counts per unit of area by the g function convolved with the areal coverage function, and with the function describing the completeness of our method, we have computed the counts predicted in our survey. With $dN(s) = [dN(s)/ds]ds$ being the number of sources detected in the flux density bin ds , $dN(s_0) = [dN(s_0)/ds_0]ds_0$ being the theoretical number of sources detected in the ‘true’ flux density bin ds_0 , and

$ds_0/ds = q_{\text{med}}/q$ (from equation 1), we have

$$\begin{aligned} \frac{dN(s)}{ds} &= \left\langle \int_0^\infty dq \left[g_A(q, f_0(s, q)) C(f_0(s, q)) \frac{dN(s_0)}{ds_0} \frac{ds_0}{ds} \right] \right\rangle \\ &= \left\langle \int_0^\infty dq \left[g_A(q, f_0(s, q)) C(f_0(s, q)) \frac{dN(s_0)}{ds_0} \frac{q_{\text{med}}}{q} \right] \right\rangle, \quad (7) \end{aligned}$$

where g_A is the convolution of the g function with the areal coverage function and C is the completeness function shown in Fig. 2. The averaging is performed over all the predicted peak flux values f_0 and with a random sampling of source positions in the survey. These expected source counts thus take into account the effects produced by the specific observational parameters of the ELAIS 15- μm survey and by our data reduction method. By putting $dN(s_0)/ds_0$ in the form given by equation (6) into equation (7), and changing s_0 to $s q_{\text{med}}/q$ (from equation 1), we obtain the source counts predicted for our survey, $dN(s)/ds$. The ratio between these counts and the theoretical source counts, $dN(s_0)/ds_0$, gives the global correction (including incompleteness and areal coverage) to be applied to our measured source counts. The inverse of the global correction (*effective area*) is reported in Fig. 3 for both S1 (top panel) and S1.5 (bottom panel) surveys. Since our source counts corrected for incompleteness were significantly different from the original model counts (especially the power law at faint flux densities), we have iterated this procedure by adjusting the power-law parameters until convergence is achieved. The final estimate of the model counts $dN(s)/ds$ is obtained for $\alpha_1 = 2.3$ and $\alpha_2 = 3.6$.

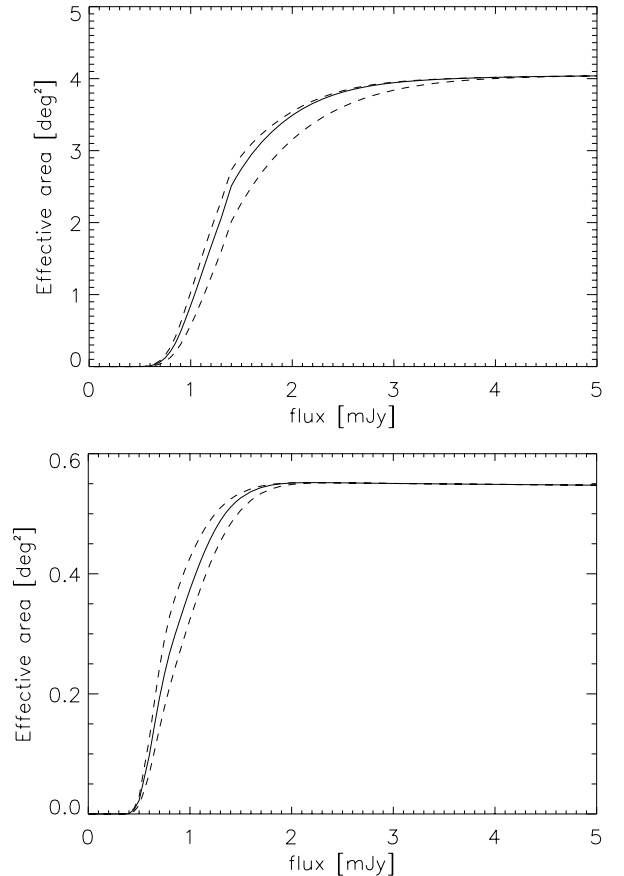


Figure 3. Effective area versus total flux density for the 15- μm catalogues in S1 main area (top) and S1.5 (bottom).

4 THE DATA SAMPLE USED FOR THE SOURCE COUNTS

The catalogue used to derive the source counts is not exactly the catalogue published in Paper I, but contains some differences, as described in this section.

First, we have conservatively decided to exclude from the source list used for counts 35 sources detected in S1, all with flux density < 1.5 mJy, that were ‘dubious’ on visual inspection of their pixel history. These sources, detected above the 5σ threshold on the maps obtained through a combination of several images, are too faint to be distinguished from noise on the single pixel histories without uncertainty. Moreover, an additional factor that strengthened our doubts about the reliability of these sources is their very low optical identification rate. In fact, while for the entire catalogue (minus the 35 ‘dubious’ sources) the optical identification rate (within a circle of 4 arcsec radius) on the DSS2 images for sources fainter than 1.5 mJy is 60 per cent, for the 35 ‘dubious’ sources it is only 14 per cent, with a chance detection rate of about 10 per cent.

Secondly, before computing the source counts we have applied three small further corrections to the flux densities presented in the catalogue of Paper I:

(i) We have applied the calibration factor of 1.096 derived from the comparison with stars in order to put our fluxes on the same scale as *IRAS* fluxes (see Section 3.1 herein and section 7 in Paper I).

(ii) We have corrected for the average underestimate of the true flux introduced by positional errors of the auto-simulated peak flux f_0 (see section 6 in Paper I). Since f_0 is computed on the measured positions and not on the ‘true’ ones, the measured flux is on average underestimated. This underestimate is flux-dependent, because of the flux dependence of positional uncertainties. In Fig. 4 the corrections to be applied to the source flux densities due to this effect are reported as a function of signal-to-noise ratio for both S1 (solid line) and S1.5 (dashed line).

(iii) In S1.5 only we have corrected for the additional loss of flux due to the combination of the three rasters. To estimate this correction factor, for each source found in the combined S1.5 map we have measured the flux in the three separate rasters and compared their average with the flux measured on the combined map. The mean ratio between the combined and the averaged single fluxes, considered as the correction factor, is $R = 0.96 \pm 0.01$.

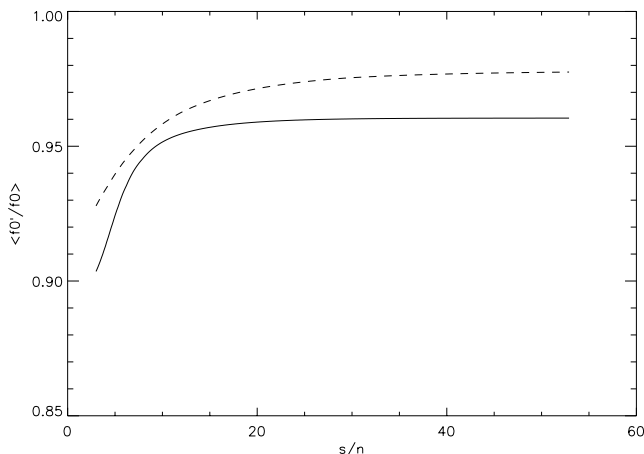


Figure 4. Correction factors as a function of signal-to-noise ratio to be applied to the S1 (solid) and S1.5 (dashed) source flux density to account for flux loss caused by positional errors in the theoretical peak flux f_0 .

In the following statistical analysis we have chosen not to eliminate the 20 repeated sources (those belonging to the overlapping regions of two different rasters), but to consider them as different sources. The reason for this choice is that the detectability and completeness analysis, and consequently the correction factors to be applied to our data, have been performed on the single raster areas. This can explain why the effective area of S1 (see Fig. 3) corresponding to bright fluxes (equal to eight times the area of one raster) is larger than the area of sky effectively covered by the S1 rasters. The sum of the effective areas shown in Fig. 3 is about 4.6 deg^2 , while the S1 + S1.5 survey covers an area of 4 deg^2 (about 15 per cent of the area is covered by at least two rasters).

Finally, to compute the extragalactic source counts, we have excluded from our lists all the sources with a stellar counterpart brighter than $B_J = 16$ in the GSC-II¹ and with an evident stellar appearance (i.e. point-like with spikes) on the DSS2² images. We have chosen not to exclude any stellar identification fainter than $B_J = 16$ found in the GSC-II (which is complete to $B_J = 19.5$), because the reddest faint stars in our sample have estimated B_J magnitude of the order of 15 (Aussel & Alexander 2001), and at fainter magnitudes the elimination from the sample of stellar-like objects might cause the elimination of active galactic nuclei (AGN) instead of stars. In fact, at $B_J \gtrsim 16$ the identifications with point-like objects are expected to be dominated by AGN.

In the end, we have identified with stars, and subtracted from our list, 82 sources in S1 and 20 in S1.5 (in total 102 stars, 87 of which are different), thus leaving a total of 325 extragalactic sources in S1 + S1.5 (320 different). The B_J magnitude (from GSC-II) distribution of these stars is reported in Fig. 5 (filled histogram), where also the magnitude distribution of all the GSC-II stars in the S1 area is reported (to $B_J = 16$). The maximum separation we find between *ISO* sources and star positions for our stellar identifications is $\lesssim 4$ arcsec, as shown in Fig. 6. Given these positional differences and the surface density of stars, we estimate that less than one *ISO*/star association could be spurious (down to the considered magnitude limit $B_J = 16$).

In Fig. 7 the fraction of stars in S1 is plotted as a function of flux density. At $S_{15\mu\text{m}} \gtrsim 50$ mJy all our sources are identified with stars and even at $S_{15\mu\text{m}} \simeq 5$ mJy the fraction of stars is $\gtrsim 50$ per cent. For this reason, an accurate star subtraction is very important before computing the extragalactic ISOCAM counts, even at relatively faint fluxes (1–2 mJy), where the fraction of stars is still of the order of 20 per cent.

In the end, the extragalactic sample used to compute the source counts composes 325 sources, 320 of which are different.

5 SOURCE COUNTS

Given the extent of the $15\text{-}\mu\text{m}$ survey in S1 and the significant depth reached in its central area, S1.5, our source sample is optimally suited to study the ISOCAM source counts with large statistics and over a broad flux range (0.5–100 mJy). Therefore, the combined sample of our S1(main area) + S1.5 non-stellar sources with $S_{15\mu\text{m}} \geq 5\sigma$ has been used to construct the mid-infrared extragalactic source counts distribution.

We used the effective areas derived in Section 3 (see Fig. 3) to obtain the extragalactic mid-infrared source counts from our $15\text{-}\mu\text{m}$

¹ The Guide Star Catalogue II is a joint project of the Space Telescope Science Institute and the Osservatorio Astronomico di Torino.

² The ‘Second Epoch Survey’ of the Southern Sky.

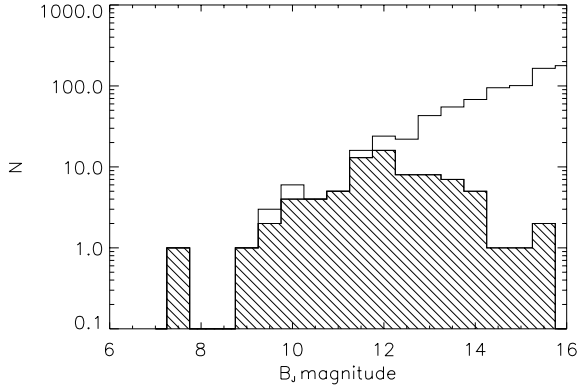


Figure 5. Magnitude distribution of our stellar identifications (cross-hatched histogram) to $B_J = 16$, compared to the magnitude distribution of all the GSC-II stars in the S1 area (empty histogram).

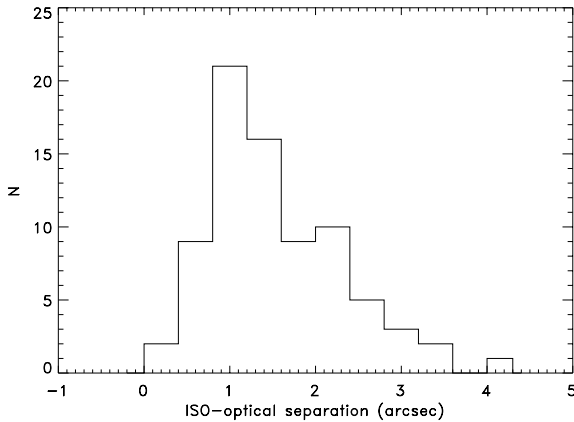


Figure 6. ISO-optical separation distribution for the stellar identifications in S1.

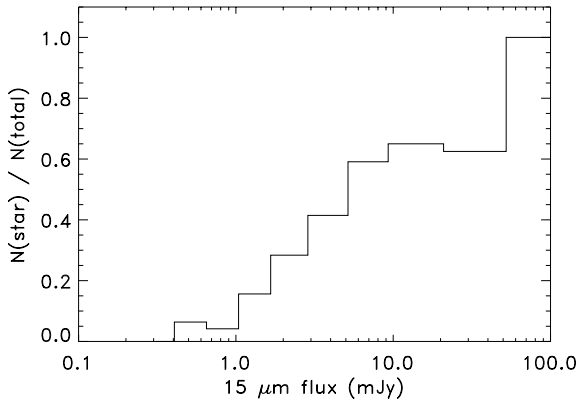


Figure 7. Ratio between stars and the total number of 15- μ m sources as a function of flux density for our S1 sample.

samples. In Table 1 the 15- μ m source counts in S1, S1.5 and S1 + S1.5 areas are presented. We have first computed the counts for the two samples in S1 and S1.5 separately, as reported in the first eight columns of Table 1, giving respectively the adopted flux density intervals, the average flux density in each interval (computed as the geometric mean of the two flux density limits), the observed number of sources, the effective area (Fig. 3, top), the differential source

counts and their associated errors in S1, and the observed number of sources, the effective area (Fig. 3, bottom) and the differential source counts with their errors in S1.5. The differential source counts have been obtained by weighting each single source for its effective area rather than weighting the total number of sources in each flux density bin for the effective area corresponding to the reference flux density of that bin. The errors associated to the counts in each bin have been computed as

$$\sqrt{\sum_i [1/A_{\text{eff}}^2(S_i)]},$$

where the sum is for all the sources with flux density S_i belonging to the bin and $A_{\text{eff}}(S_i)$ is the effective area corresponding to that source flux. These errors take into account only the Poisson term of the uncertainties associated to the source counts, for consistency with other literature work. Especially at faint flux density, where the effective area (and consequently the correction factor) is a steep function of flux, the errors quoted in Table 1 should be considered as lower limits of the ‘true’ errors (including also the uncertainty in the effective area computation, shown as dashed curves in Fig. 3).

The counts computed for S1 and S1.5 are consistent within the errors in most flux density intervals, the only exception being the 0.8–1.2 mJy flux bin, where the counts in S1 are larger than the ones in S1.5 at a formal level of $\sim 2.3\sigma$. However, since the low flux density errors are somewhat underestimated, we can consider the source counts in S1 and S1.5 consistent in all the common flux density intervals, over the whole range 0.5–100 mJy.

For this reason, we have also computed the source counts in the ‘combined’ sample (S1 + S1.5), by considering all the sources as belonging to a unique sample: for each source the combined effective area is the sum of the effective areas in S1 and S1.5 (whose values are reported in columns 4 and 7 respectively). In the last four columns, the total number of sources in each flux density bin, the differential source counts, the differential counts normalized to the Euclidean distribution (by multiplying by $\langle s \rangle^{2.5}$) with their errors and the integral source counts (with errors) for the combined sample are reported. In the first flux density bin the counts for the combined sample coincide with the S1.5 counts, since, because of their negligible effective area, we have not considered the S1 data.

Note that the flux bins are partially overlapping, and therefore they are not statistically independent (they are alternately independent). The choice of partially overlapping flux density bins for our source counts representation is based on the need for a tight sampling of the region where the counts start diverging from no-evolution models, in order to better determine the break point and the counts shape (with larger statistics). As mentioned in the previous section, in computing the counts we have considered as two different sources those appearing in two different rasters (belonging to the border part of a raster, overlapping with an adjacent raster), by suitably weighting them for their detectability area in each raster. In fact, in deriving the areal coverage function we have considered the total area of each single raster, including the overlapping regions.

The 15- μ m differential source counts of the combined ELAIS S1 and S1.5 data, normalized to those expected in a Euclidean geometry by dividing by $S^{-2.5}$, are shown in Fig. 8 (filled stars). For comparison, source counts from other ISOCAM surveys [A2390 from Altieri, Metcalfe & Kneib (1999); *ISO Hubble Deep Field North* (HDF-N) from Aussel et al. (1999a); *ISO Hubble Deep Field South* (HDF-S), Marano Fierback, Marano Ultra-Deep, Marano Deep, Lockman Deep and Lockman Shallow from Elbaz et al. (1999b); data kindly provided by D. Fadda, private communication] are also

Table 1. The 15- μ m source counts in S1 + S1.5.

S (mJy)	$\langle S \rangle$ (mJy)	n	S1 A_{eff} (deg ²)	dn/dS (deg ⁻² mJy ⁻¹)	n	S1.5 A_{eff} (deg ²)	dn/dS (deg ⁻² mJy ⁻¹)	n	dn/dS (deg ⁻² mJy ⁻¹)	S1 + S1.5 (dn/dS) $S^{2.5}$ (deg ⁻² mJy ^{1.5})	$N(>S)$ (deg ⁻²)
0.50–0.80	0.63	6	0.02	–	19	0.13	1344 \pm 539	19	1344 \pm 539	428 \pm 171	544 \pm 163
0.63–1.01	0.80	34	0.21	672 \pm 157	27	0.27	521 \pm 113	61	645 \pm 109	369 \pm 62	353 \pm 42
0.80–1.28	1.01	76	0.90	380 \pm 59	21	0.38	161 \pm 36	97	280 \pm 33	288 \pm 34	194 \pm 17
1.01–1.62	1.28	88	2.00	127 \pm 5	19	0.48	81 \pm 19	107	116 \pm 12	215 \pm 22	108 \pm 8
1.28–2.05	1.62	77	2.94	44 \pm 5	19	0.54	51 \pm 12	96	45 \pm 5	152 \pm 16	59.6 \pm 4.4
1.62–2.75	2.11	67	3.57	18 \pm 2	16	0.54	26 \pm 7	83	20 \pm 2	126 \pm 14	37.8 \pm 3.1
2.05–3.69	2.75	50	3.85	8.1 \pm 1.2	10	0.54	11 \pm 4	60	8.6 \pm 1.1	108 \pm 14	24.7 \pm 2.4
2.75–4.95	3.69	34	4.00	3.9 \pm 0.7	4	0.54	3.3 \pm 1.7	38	3.9 \pm 0.6	101 \pm 16	15.8 \pm 1.9
3.69–6.64	4.95	24	4.00	2.0 \pm 0.4	2	0.54	1.2 \pm 0.9	26	1.9 \pm 0.4	105 \pm 21	10.6 \pm 1.5
4.95–8.90	6.64	18	4.00	1.1 \pm 0.3	1	0.54	0.5 \pm 0.5	19	1.1 \pm 0.2	120 \pm 28	7.3 \pm 1.3
6.64–11.9	8.90	11	4.00	0.5 \pm 0.2	0	0.54	0.0 \pm 0.0	11	0.5 \pm 0.1	109 \pm 33	4.9 \pm 1.0
8.90–18.9	13.0	7	4.00	0.2 \pm 0.1	1	0.54	0.2 \pm 0.2	8	0.2 \pm 0.1	106 \pm 38	3.1 \pm 0.8
11.9–29.9	18.9	5	4.00	0.07 \pm 0.03	2	0.54	0.2 \pm 0.1	7	0.09 \pm 0.03	133 \pm 50	2.2 \pm 0.7
18.9–47.2	29.9	2	4.00	0.02 \pm 0.01	1	0.54	0.1 \pm 0.1	3	0.02 \pm 0.01	113 \pm 65	1.1 \pm 0.5
29.9–74.6	47.2	3	4.00	0.02 \pm 0.01	0	0.54	0.0 \pm 0.0	3	0.02 \pm 0.01	225 \pm 130	0.7 \pm 0.4
47.2–118.0	74.6	2	4.00	0.007 \pm 0.005	0	0.54	0.0 \pm 0.0	2	0.006 \pm 0.004	298 \pm 211	0.4 \pm 0.3

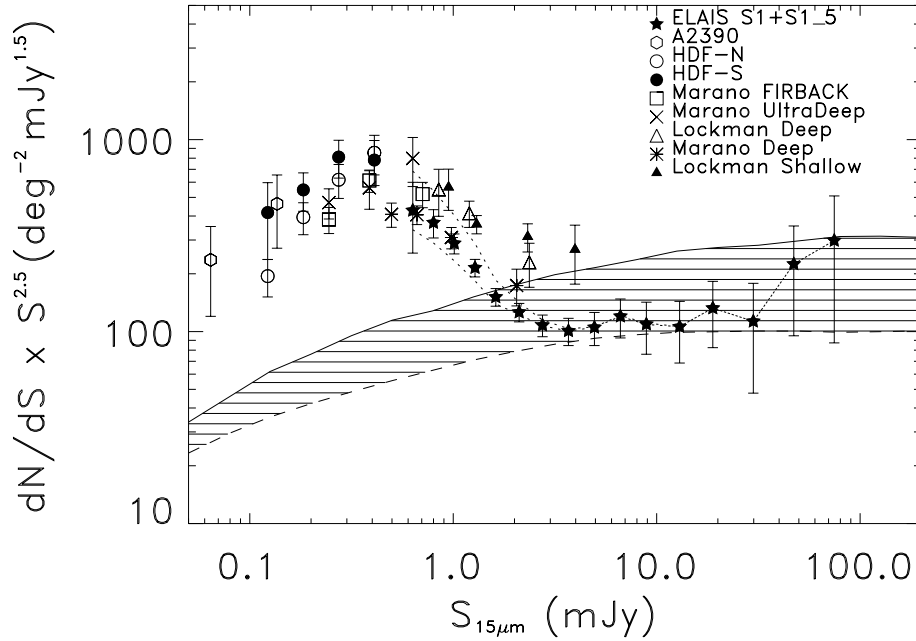


Figure 8. Differential source counts at 15 μ m normalized to the Euclidean distribution [$N(S) \propto S^{-2.5}$]. Data points (as shown also in the figure): A2390 (open diamonds), *ISO* HDF-N (open circles), *ISO* HDF-S (filled circles), Marano Firback (open squares), Marano Ultra-Deep (diagonal crosses), Marano Deep (asterisks), Lockman Deep (open triangles), Lockman Shallow (filled triangles), ELAIS S1 (filled stars). The dotted curves are the lower and upper envelopes of our counts due to the uncertainties in the completeness curve derivation, as shown in Fig. 3. The hatched area represents the range of possible expectations from no-evolution models normalized to the *IRAS* 12- μ m local luminosity function (upper limit from Rush et al. 1993, lower limit from Fang et al. 1998).

plotted. Our counts are lower than the Lockman Deep and Shallow ones. However, they appear consistent with the counts obtained in the Marano Deep Survey, at least in the common flux density range (0.5–2 mJy).

In Fig. 9 our integral extragalactic source counts are reported. The grey-shaded area shows the integral extragalactic counts with 68 per cent confidence contours obtained from the ELAIS S1 + S1.5 survey. For comparison, the black-shaded area represents the

counts with 68 per cent confidence contours obtained from the ISOCAM deep/ultra-deep surveys (Elbaz et al. 1999b). The hatched area represents the integral counts of Serjeant et al. (2000) based on the preliminary analysis of the whole ELAIS survey, with fluxes rescaled downwards by an average factor of 2, as suggested by a recent calibration work (Väisänen et al. 2002). The area filled with horizontal lines represents the range of possible expectations from no-evolution models normalized to the *IRAS* 12- μ m local

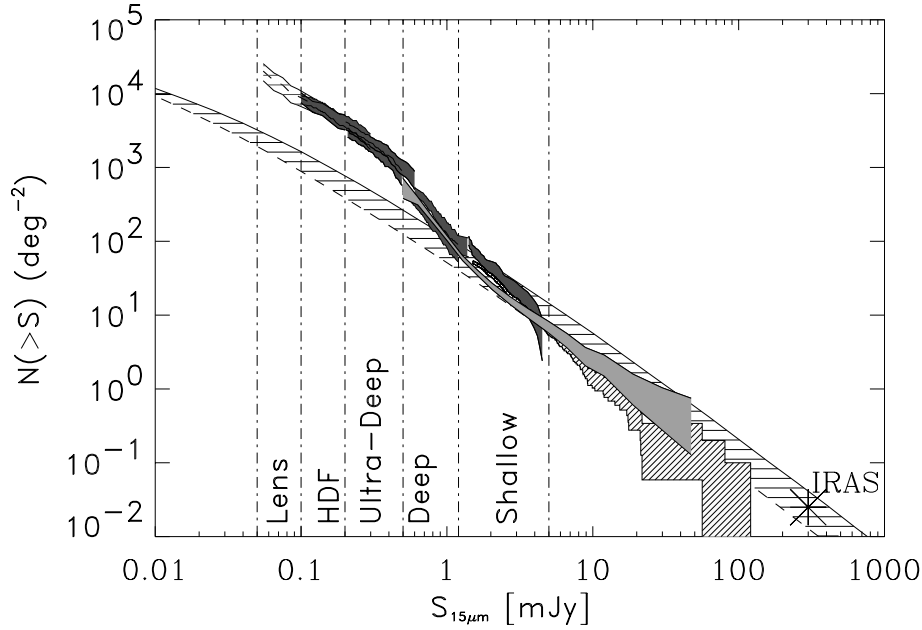


Figure 9. Integral source counts for extragalactic ISOCAM sources detected at 15 μm above a given flux S . The grey-shaded area shows the integral extragalactic counts with 68 per cent confidence contours obtained from the ELAIS S1 survey (this work). For comparison, the cross-hatched and the black-shaded areas represent the counts with 68 per cent confidence contours obtained respectively from the ELAIS preliminary analysis, normalizing downwards by a factor of 2 the fluxes of Serjeant et al. (2000), and from the ISOCAM deep/ultra-deep surveys (Elbaz et al. 1999b). The area filled with horizontal lines represents the range of possible expectations from no-evolution models normalized to the *IRAS* 12- μm local luminosity function, as reported in Fig. 8. The fainter end of the *IRAS* 12- μm source counts derived by Rush et al. (1993), converted to 15 μm , is represented by the asterisk.

luminosity function. The asterisk represents the fainter end of the *IRAS* 12- μm source counts derived by Rush, Malkan & Spinoglio (1993), opportunely converted to 15 μm .

Our data reduction allowed us to compute source counts down to fluxes ~ 3 times fainter than the preliminary analysis (PA) of the ELAIS data (Serjeant et al. 2000). In the flux range common to the two samples, we find that, after correcting the PA fluxes downwards by a factor of 2, our source counts are in reasonably good agreement with the counts of Serjeant et al. (2000) above ~ 2.5 mJy. However, the overall slope of the Serjeant et al. counts appears to be steeper than ours, with our counts being lower below 2.5 mJy and somewhat higher above 10 mJy. This is probably due the fact that a flux-dependent calibration correction, rather than a constant correction, should be applied to the Serjeant et al. (2000) fluxes. In fact, there are hints (Babbedge & Rowan-Robinson, in preparation) that the needed correction factor is ~ 2.4 for the fainter PA fluxes and ~ 1.75 for the brighter fluxes (the factor of 2 here adopted is an average value).

Our counts, though not deep enough to detect the fast convergence at flux densities fainter than 0.4 mJy shown by the deep/ultra-deep ISOCAM counts, sample very well the flux density range where those counts start diverging from no-evolution models. Indeed, we observe a remarkable change in the slope of our counts, showing a significant super-Euclidean slope from about 2 mJy to ~ 0.45 mJy. Owing to its large statistics, our survey is at the moment best suited for determining both the exact flux density where the 15- μm extragalactic counts steepen and the count slope itself (before and after the steepening). A maximum likelihood fit to our extragalactic source counts with two power laws,

$$\frac{dN}{dS} \propto \begin{cases} S^{-\alpha_1} & \text{if } S > S_b, \\ S^{-\alpha_2} & \text{if } S < S_b, \end{cases} \quad (8)$$

gives the following parameters: $\alpha_1 = 2.35 \pm 0.05$, $\alpha_2 = 3.60 \pm 0.05$, $S_b = 2.15 \pm 0.05$ mJy. Our best-fitting parameters suggest that the steepening of the integral counts starts around 2 mJy, then the counts keep a super-Euclidean slope down to the limits of our survey (~ 0.5 mJy).

6 DISCUSSION

6.1 Comparison with deep/ultra-deep ISOCAM survey source counts

The 15- μm extragalactic source counts derived from the ELAIS Southern survey cover over two decades in flux, from 0.5 up to 100 mJy, with a significant statistical sampling (325 objects). Owing to the large flux density interval covered, the ELAIS counts bridge the gap existing between the *IRAS* counts and the ISOCAM deep/ultra-deep counts. The ELAIS survey was planned to be a shallow survey and to reach an optimistic limit of about 2 mJy. As shown in Paper I, with the Lari technique we were able to go much deeper than expected, detecting a significant number of sources even at sub-milliJansky levels. The strength of ELAIS counts is at fluxes brighter than ~ 1 mJy, where they are highly statistically significant and complete. At fainter fluxes, though the S1 and S1.5 counts are consistent over the whole flux range, the results are less strong as a result of the large incompleteness correction required by the S1 data and the small area covered by the more complete S1.5 data. However, the results are consistent with the evolution scenario found by other ISOCAM surveys and are able to give general hints on the behaviour and evolution of infrared galaxies. In particular, ELAIS counts in the flux density range in common with ISOCAM deep counts (0.5–4 mJy) diverge from no-evolution models as well and steepen with a super-Euclidean slope (3.60 ± 0.05

for the differential form) up to the fainter limit. In particular, the flux density where our counts start diverging from no-evolution predictions is 2.15 ± 0.05 mJy. Above this flux density, the ELAIS counts are consistent with no evolution, showing a slope (in differential form) of 2.35 ± 0.05 . Although similar results have been found for the deep ISOCAM surveys, between 0.5 and ~ 2 mJy our counts are somewhat steeper and on average lower than the others. However, the common flux range is sampled by three deep surveys only: Marano Deep, Lockman Deep and Lockman Shallow. The counts drawn from the Marano Deep survey appear consistent with the ELAIS counts, while the counts obtained from both Lockman Deep and Shallow surveys are less steep at faint fluxes (especially the Lockman Shallow ones) and higher than ours by about a factor of 2–3 around 2–3 mJy.

The reason for this discrepancy is still not completely understood. It could be due to different separate causes or to a combination of them. A possible reason might be attributed to the different data reduction methods applied to different surveys. For example, our survey has been reduced with the Lari method (see Paper I), while the Marano and the Lockman Deep surveys have been reduced with the Preti method (Starck et al. 1999) and the Lockman Shallow survey has been reduced with the triple beam switch method of IAS (Désert et al. 1999). We must note that the Preti method was especially designed to account for all the spurious effects of ISOCAM data in a more complete way than the triple beam switch method. A comparison between these two methods performed in the HDF-N (Aussel et al. 1999a) has produced similar results, although not all the sources detected by one method were present in the list found by the other method. Moreover, flux densities derived for the common sources with the triple beam switch method were systematically lower, by a factor of 0.82, than the Preti fluxes. In fact, each method measures fluxes in a different way (i.e. auto-simulations for Lari, photometry aperture plus implicit colour correction for Preti, fit with a fixed-width Gaussian for the triple beam switch), and this might produce small differences in the photometry of the objects. However, if our fluxes were on the same scale as the Preti ones, the assumption that the triple beam switch fluxes are 20 per cent lower would further increase the observed discrepancy between our counts and the Lockman Shallow counts. Vice versa, good agreement between Lockman Deep counts and our counts would be obtained if the Lockman Deep fluxes were systematically higher than ours by about 15 per cent (see Fig. 10). The flux calibration of our cata-

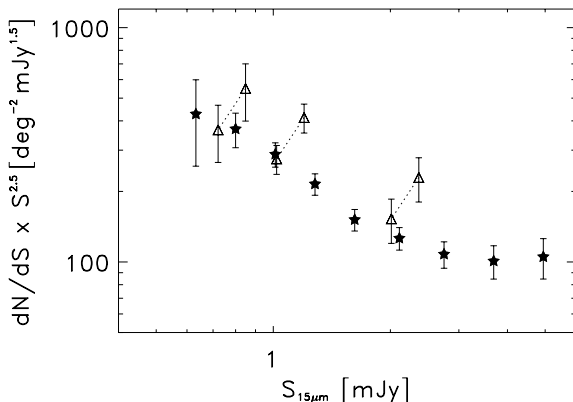


Figure 10. Zoom of the normalized differential source counts at 15 μm . The symbols are the same as in Fig. 8: filled stars for ELAIS counts and open triangles for Lockman Deep counts. The upper Lockman points are the original counts, while the lower ones are the counts obtained with 15 per cent lowered fluxes.

logue, as described in detail in Paper I, has been tested using the stars in the field and resulted in the same flux scale as *IRAS* (relative flux scale of 1.096 ± 0.044), with photometric errors not larger than 10 per cent.

Another possible cause of the counts difference could be an incomplete star subtraction performed in the Lockman surveys, whose brightest flux density bins (at 2–5 mJy) might contain between 20 and 50 per cent of stars (as shown in Section 5).

Finally, part of the observed discrepancy could also be due to cosmic variance affecting small area fields, like the Marano Deep Field (0.2 deg^2) and the Lockman Deep and Shallow Fields (respectively 0.14 and 0.54 deg^2).

6.2 Models and interpretation

As already mentioned, at flux densities $\gtrsim 1$ –2 mJy, the ELAIS counts are consistent with the expectation of models assuming no evolution for extragalactic sources, while they strongly depart from no-evolution predictions at fainter fluxes. The almost flat differential counts (normalized to Euclidean) extending from the *IRAS* fluxes to 1–2 mJy, followed by the sudden upturn below, seem to require strong evolution for a single population rather than for the whole population of 15- μm galaxies.

Owing to the uncertainties existing in our counts at faint fluxes, in this paper we do not pretend to construct an evolutionary model based on our result. However, in order to interpret our data and the evolution they seem to require, we have compared our counts with recent evolution models for mid-infrared galaxies found in the literature. In particular, we have compared our counts with the models of Xu (2000) and Franceschini et al. (2001). Neither model is able to reproduce the sharp departure feature from no-evolution predictions, or the low ‘plateau’ between 1–2 and 100 mJy shown by our data. The Xu (2000) model is able to fit the deep/ultra-deep ISOCAM counts by considering a rather extreme luminosity evolution, i.e. $L(z) = L(0) \times (1+z)^{4.5}$, for the whole infrared population. However, it largely overpredicts our counts above 0.8–1 mJy and its departure from no-evolution predictions is far too smooth to reproduce the sharp upturn shown by our data around 2 mJy. The model predictions of Franceschini et al. (2001) are somewhat steeper than the Xu ones, but still overestimating and smoother than our counts, though considering a combination of luminosity and density evolution for star-forming galaxies only. The local luminosity functions (LLFs) on which these models are based are different: the one considered by Xu (2000) has been derived using the bivariate (15- μm versus 60- μm luminosities) method, from an *IRAS* sample selected at 60 μm and observed by ISOCAM at 15 μm , while the one used by Franceschini et al. (2001) is an adapted combination of the 12- μm LLF from Fang et al. (1998) and the bivariate 15–60 μm , converted to 12 μm , from Xu et al. (1998). Franceschini et al. (2001) have also tried to disentangle the contributions of different populations. Because of its greater flexibility in allowing one to play with the different populations and their evolutionary properties, we have based our analysis on the Franceschini et al. (2001) models, trying to find a good fit to our data by varying the LLF free parameters.

These models are able to reproduce the deep/ultra-deep ISOCAM counts by considering different evolutionary properties for three different populations: non-evolving normal spirals, strongly evolving starburst plus type 2 Seyfert galaxies, and evolving type 1 active galactic nuclei (AGN 1). The latter are assumed to evolve in luminosity as $L(z) = L(0) \times (1+z)^3$ up to $z = 1.5$ and constant luminosity density at higher redshift. For the population

of star-forming and type 2 Seyfert galaxies, in a $H_0 = 50 \text{ km s}^{-1} \text{ Mpc}^{-1}$, $\Omega_m = 0.3$, $\Omega_\Lambda = 0.7$ universe, the best fit to deep/ultra-deep ISOCAM counts is found by Franceschini et al. (2001) by considering luminosity evolution $L(z) = L(0) \times (1+z)^{3.8}$ and density evolution $\rho(L(z), z) = \rho_0(L) \times (1+z)^4$ up to $z_{\text{break}} = 0.8$, and no additional evolution at $z > z_{\text{break}}$.

We have changed neither the evolution (form and rate) for AGN 1, nor the evolutionary scheme for star-forming (plus type 2 Seyfert) galaxies. However, for the latter, we have varied the luminosity and density evolution rates (respectively α_L and α_D hereafter), z_{break} and the LLF normalization. The crucial point is the star-forming galaxy LLF and in particular its shape at bright luminosities. In order to fit the sharp rise of our counts below 2 mJy, we have found it essential to introduce a luminosity break (L_{break}) in the star-forming LLF, above which it quickly drops to zero. This is also strongly required by the redshift distribution for bright sources (above a few millijansky). In fact, without any luminosity break in the LLF, the redshift distribution predicted by the Franceschini et al. (2001) model, for example for sources brighter than 5 mJy, shows a significant secondary peak around $z \sim 1$, in addition to a low-redshift peak. This is not consistent with the redshifts measured for bright ELAIS sources ($S \geq 2 \text{ mJy}$; Gruppioni et al. 2001; La Franca et al., in preparation), which are all found to be at rather low redshifts ($z < 0.3\text{--}0.4$).

We have taken into account the redshift distribution constraints when looking for the best fit to our observed source counts. In particular, we have required the model results to agree roughly with the following observational evidence:

- (i) Absence of high-redshift peak for bright ($\geq 2 \text{ mJy}$) sources (Gruppioni et al. 2001; La Franca et al., in preparation).
- (ii) Majority of sources at moderate redshifts ($z < 0.3\text{--}0.4$) even at fluxes $S \geq 0.8\text{--}1 \text{ mJy}$, with a fraction of high- z sources not larger than 30–35 per cent (Pozzi et al., in preparation).
- (iii) Redshift distribution for deep surveys ($S \geq 0.1\text{--}0.2 \text{ mJy}$) showing a peak between $z = 0.5$ and $z = 1.2$ (HDF-N: Aussel et al.

1999b; Aussel et al., in preparation, as reported by Franceschini et al. 2001; CFRS 1415 + 52: Flores et al. 1999).

The best solution was found for $\alpha_L = 3.0$, $\alpha_D = 3.5$, $z_{\text{break}} = 1.1$, a LLF of evolving starburst population 40 per cent higher than the Franceschini one and $L_{\text{break}} = 10^{10.8} L_\odot$. In Fig. 11 the fit to source counts obtained with the above parameters is shown, while the redshift distributions expected for our survey at $S_{15\mu\text{m}} \geq 0.1, 1.0$ and 2.0 mJy are plotted in Fig. 12. These distributions are in good agreement with the preliminary results of optical identification for the S1 sources on the DSS2. We find, in fact, that, while above 2 mJy most sources have an optical counterpart brighter than $R \simeq 21.5$ (92 per cent at $S_{15\mu\text{m}} \geq 2 \text{ mJy}$ and 95 per cent at $S_{15\mu\text{m}} \geq 3 \text{ mJy}$), between 1 and 2 mJy there is a quick drop in the identification fraction (it goes down to ~ 70 per cent), probably associated with a change in population (i.e. the appearance of a high- z excess number of sources in the redshift distribution). At $S_{15\mu\text{m}} \geq 1 \text{ mJy}$, the expected high- z ($z \geq 0.6$) fraction of sources is ~ 35 per cent, in good agreement with the fraction of S1 sources to the same flux density without optical counterpart on the DSS2.

Our result shows that significant evolution is needed for at least a class of extragalactic objects, in order to explain the observed source counts below a few millijansky. Above about 10 mJy the counts are dominated by a non-evolving population of normal spiral galaxies, while below this flux density a population of strongly evolving starburst galaxies shows up and, rapidly rising, starts dominating the counts. At fluxes $\lesssim 3\text{--}5 \text{ mJy}$, evolving starburst galaxies make up most of the observed counts, being responsible for the peak around $0.3\text{--}0.4 \text{ mJy}$ revealed by the deep and ultra-deep ISOCAM surveys. The evolution required for this class of objects is lower than found by Franceschini et al. (2001): α_L is 3.0 instead of 3.8 and α_D is 3.5 instead of 4.0. However, a turnover at higher z ($z_{\text{break}} = 1.1$ instead of 0.8) is needed in order to reproduce both the sharp rise of our counts and the faint flux peak of the deep ISOCAM survey counts. This value for z_{break} is intermediate between the 0.8 found by

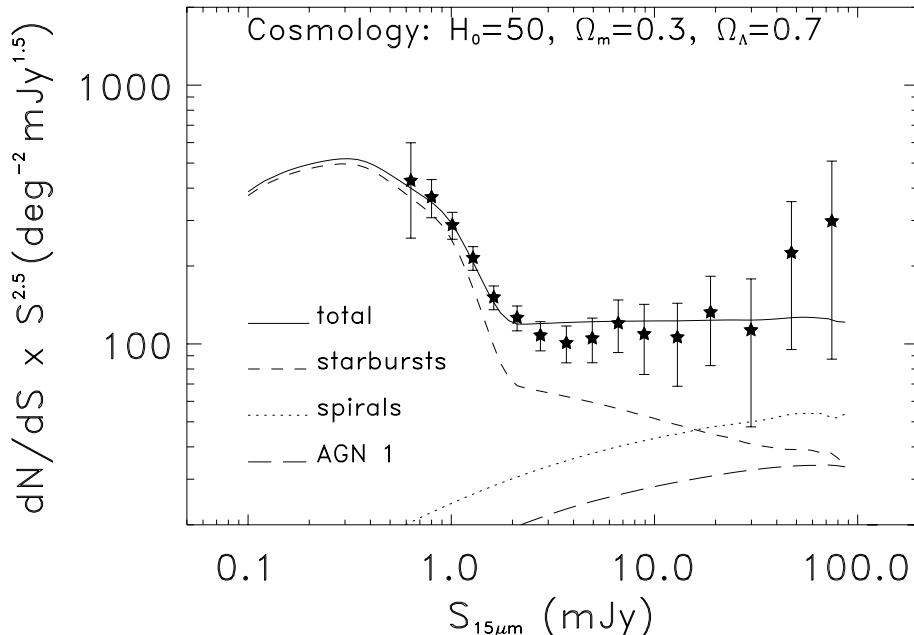


Figure 11. Best-fitting model (re-adapted from Franceschini et al. 2001) to ELAIS S1 source counts. The dotted line corresponds to the expected counts for a population of non-evolving spirals. The short-dashed line is the modelled contribution of a population of strongly evolving starburst (plus type 2 Seyfert) galaxies, while the long-dashed line is the contribution of type 1 AGN. The solid line represents the expected total source counts.

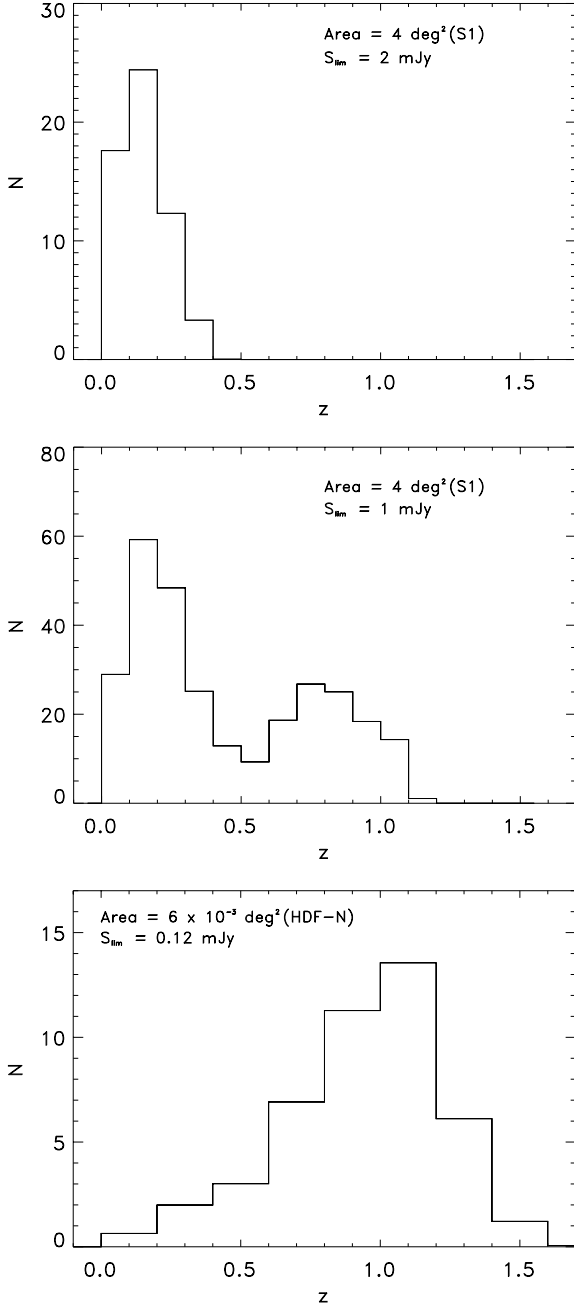


Figure 12. Redshift distributions predicted by our best-fitting model for 15- μ m sources at different flux levels and in different areas. Top: $S \geq 2$ mJy, area = 4 deg² (S1). Middle: $S \geq 1$ mJy, area = 4 deg² (S1). Bottom: $S \geq 0.12$ mJy, area = 6×10^{-3} deg² (HDF-N). The latter is computed for the HDF-N area and to the same flux limit for a direct comparison with the redshift distribution observed in that field (Aussel et al., in preparation).

Franceschini et al. (2001) and 1.5 found by Xu (2000), though the latter obtains a reasonably good fit to the deep/ultra-deep counts and to the redshift distribution of ISOCAM sources in the HDF-N (Aussel et al. 1999b), by considering pure luminosity evolution (with $\alpha_L = 4.5$) for the whole 15- μ m extragalactic population. However, the Xu (2000) model is not able to fit the new redshift distribution observed in the HDF-N with >90 per cent complete spectroscopic identification, as derived by Aussel et al. (in preparation) and reported by Franceschini et al. (2001).

We have obtained an estimate of the 15- μ m CIRB flux by directly integrating the best-fitting model counts down to $S_{15\mu\text{m}} = 50 \mu\text{Jy}$: $2.2 \text{ nW m}^{-2} \text{ sr}^{-1}$. This value is in good agreement with the computation done by Elbaz et al. (2002, as reported by Chary & Elbaz 2001), who find a value of $2.4 \pm 0.5 \text{ nW m}^{-2} \text{ sr}^{-1}$ by integrating the observed ISOCAM deep/ultra-deep counts down to the same flux density limit. Our estimate of the 15- μ m CIRB flux corresponds to about 67 per cent of the total resolved CIRB at 15 μ m derived by Biviano et al. (2000) as $3.3 \pm 1.3 \text{ nW m}^{-2} \text{ sr}^{-1}$.

7 CONCLUSIONS

ISOCAM extragalactic source counts in the flux density range 0.5–100 mJy have been derived for the ELAIS 15- μ m samples obtained in the Southern hemisphere area with a new data reduction technique (see Paper I). Our counts sample very well the flux density region where deep/ultra-deep ISOCAM counts start diverging from no-evolution models. Indeed, we observe a significant change in slope from a value of ~ 2.35 at fluxes higher than $S \simeq 2$ mJy to a very steep value ($\alpha \sim 3.60$) for fainter fluxes down to our flux limit ($S \simeq 0.5$ mJy).

This is in qualitative agreement with previous results, although the ELAIS counts show a somewhat steeper slope at faint fluxes than the other surveys ($\alpha \simeq 3.0$ between 0.4 and 4 mJy; Elbaz et al. 1999b). At the faintest limit of our survey ($S \sim 0.5$ –1.0 mJy), where data from a number of other surveys exist, our counts agree with those obtained in the Marano Deep survey and are somewhat lower than those obtained in other surveys. At brighter fluxes ($S \gtrsim 2$ –5 mJy), where our data are highly complete and statistically significant (because of the large sampled area), our counts are significantly lower than the counts in the Lockman Deep and Shallow surveys. The observed difference might be attributable to the different reduction methods applied to different surveys, to incomplete star subtractions and to cosmic variance that could affect small area surveys (i.e. Lockman Deep and Shallow, Marano Deep).

A good fit to our counts is obtained by re-adapting the Franceschini et al. (2001) model and introducing a luminosity break in the local luminosity function of the evolving population. Our solution considers no evolution for normal spiral galaxies (dominating the counts at fluxes $\gtrsim 5$ –10 mJy), a combination of luminosity and density evolution [$L(z) = L(0) \times (1+z)^{3.0}$ and $\rho(L(z), z) = \rho_0(L) \times (1+z)^{3.5}$] up to $z_{\text{break}} = 1.1$ for starburst galaxies, with a break in their LLF at $L_{15\mu\text{m}} = 10^{10.8} L_{\odot}$, and luminosity evolution [$L(z) = L(0) \times (1+z)^{3.0}$ up to $z = 1.5$] for AGN 1. Strongly evolving starburst galaxies rise quickly below ~ 10 mJy and start making up almost the totality of the observed counts at fluxes fainter than a few milliJansky. Our results are also in agreement with the observed redshift distributions at different flux levels (from 10 down to 0.1 mJy), predicting a rather local population ($z_{\text{med}} \simeq 0.2$) of star-forming galaxies down to ~ 1.5 mJy and a rapid rise of a high- z ($z_{\text{med}} \simeq 1$) excess of objects at fainter flux densities. This high- z population totally dominates below ~ 0.5 mJy.

ACKNOWLEDGMENTS

This work was supported by the EC TMR Network programme FMRX-CT96-0068. CG acknowledges partial support by the Italian Space Agency under the contract ASI-I/R/27/00 and by the Italian Ministry for University and Research (MURST) under grant COFIN99. The authors thank D. Fadda for kindly providing the counts data relative to deep and ultra-deep ISOCAM surveys.

The Guide Star Catalogue II is a joint project of the Space Telescope Science Institute (STScI) and the Osservatorio Astronomico di Torino. The STScI is operated by the Association of Universities for Research in Astronomy, for the National Aeronautics and Space Administration under contract NASS-26555. The participation of the Osservatorio Astronomico di Torino is supported by the Italian Council for Research in Astronomy. Additional support is provided by European Southern Observatory, Space Telescope European Coordinating Facility, the International GEMINI project and the European Space Agency Astrophysics Division.

The ‘Second Epoch Survey’ (DSS2) of the Southern Sky was made by the Anglo–Australian Observatory (AAO) with the UK Schmidt Telescope. Plates from this survey have been digitized and compressed by the STScI. The digitized images are copyright © 1993–1995 by the AAO Board and are distributed herein by agreement. All rights reserved.

REFERENCES

- Alexander D. M. et al., 2001, *ApJ*, 554, 18
- Altieri B., Metcalfe L., Kneib J. P., 1999, *A&A*, 343, L65
- Aussel H., Alexander D. M., 2001, *A&AS*, 198, 4910
- Aussel H., Césarsky C. J., Elbaz D., Starck J.-L., 1999a, *A&A*, 342, 313
- Aussel H., Elbaz D., Césarsky C. J., Starck J.-L., 1999b, in Cox P., Kessler M. F., eds, *ESA Spec. Publ. Ser. SP-427, The Universe as Seen by ISO*. ESA Publications Division, Noordwijk, p. 1023
- Biviano A. et al., 2000, in Mazure A., Le Fèvre O., Le Brun V., eds, *ASP Conf. Ser. Vol. 200, Clustering at High Redshift*. Astron. Soc. Pac., San Francisco, p. 101 (astro-ph/9910314)
- Cesarsky C. J. et al., 1996, *A&A*, 315, L32
- Chary R., Elbaz D., 2001, *ApJ*, 556, 562
- Désert F.-X., Puget J.-L., Clements D. L., Péroult M., Abergel A., Bernard J.-P., Cesarsky C. J., 1999, *A&A*, 342, 363
- Dole H. et al., 1999, in Cox P., Kessler M. F., eds, *ESA Spec. Publ. Ser. SP-427, The Universe as Seen by ISO*. ESA Publications Division, Noordwijk, p. 1031
- Elbaz D., 2000, in Hammer F., Thuan T. X., Cayatte V., Guiderdoni B., Tran Thanh Van J., eds, *Building Galaxies: From the Primordial Universe to the Present*. Editions Frontières, Gif-sur-Yvette, p. 195
- Elbaz D. et al., 1999a, in Cox P., Kessler M. F., eds, *ESA Spec. Publ. Ser. SP-427, The Universe as Seen by ISO*. ESA Publications Division, Noordwijk, p. 999
- Elbaz D. et al., 1999b, *A&A*, 351, L37
- Elbaz D., Cesarsky C. J., Chanial D., Aussel H., Franceschini F., Fadda D., Chary L., 2002, *A&A*, 384, 848
- Fang F., Shupe D., Xu C., Hacking P., 1998, *ApJ*, 500, 693
- Fixsen D. J., Dwek E., Mather J. C., Bennett C. L., Shafer R. A., 1998, *ApJ*, 508, 123
- Flores H. et al., 1999, *ApJ*, 517, 148
- Franceschini A., Aussel H., Cesarsky C. J., Elbaz D., Fadda D., 2001, *A&A*, 378, 1
- Gruppioni C. et al., 1999, *MNRAS*, 305, 297
- Gruppioni C., Pozzi F., Ciliegi P., Mignoli M., La Franca F., Oliver S., Rowan-Robinson M., 2001, in Van Bemmell I., Barthel P., Wilkes B., eds, *New Astron. Rev. Ser., The Far-Infrared and Sub-Millimeter Spectral Energy Distributions of Active and Starburst Galaxies*. Elsevier, Amsterdam, available at <http://www.elsevier.com/locate/astrev>
- Hacking P. B., Houck J. R., Condon J. J., 1987, *ApJ*, 316, 15
- Hauser M. G., Arendt R. G., Kelsall T., 1998, *ApJ*, 508, 25
- Kessler M. F. et al., 1996, *A&A*, 315, 27
- Kim D. B., Sanders D. B., 1998, *ApJS*, 119, 41
- Lagache G., Abergel A., Boulanger F., Désert F. X., Puget J.-L., 1999, *A&A*, 344, 322
- Lari C. et al., 2001, *MNRAS*, 325, 1173 (Paper I)
- Lilly S., Le Fèvre O., Hammer F., Crampton D., 1996, *ApJ*, 460, L1
- Lonsdale C. J., Hacking P. B., 1989, *ApJ*, 339, 712
- Metcalfe N., Shanks T., Fong R., Roche N., 1995, *MNRAS*, 273, 257
- Oliver S. et al., 2000, *MNRAS*, 316, 749
- Puget J.-L., Abergel A., Bernard J.-P., Boulanger F., Burton W. B., Désert F.-X., Hartmann D., 1996, *A&A*, 308, L5
- Rowan-Robinson M., 2001, *ApJ*, 549, 745
- Rush B., Malkan M. A., Spinoglio L., 1993, *ApJS*, 89, 1
- Saunders W., Rowan-Robinson M., Lawrence A., Efstathiou G., Kaiser N., Ellis R. S., Frenk C. S., 1990, *MNRAS*, 242, 318
- Serjeant S. et al., 2000, *MNRAS*, 316, 768
- Soifer B. T., Neugebauer G., 1991, *AJ*, 101, 354
- Starck J.-L., Aussel H., Elbaz D., Fadda D., Cesarsky C., 1999, *A&AS*, 138, 365
- Väisänen P. et al., 2002, *MNRAS*, submitted
- Xu C., 2000, *ApJ*, 541, 134
- Xu C. et al., 1998, *ApJ*, 508, 576

This paper has been typeset from a \LaTeX file prepared by the author.